Journal of Materials Chemistry A

PAPER

View Article Online
View Journal | View Issue

Cite this: J. Mater. Chem. A, 2014, 2, 7319

Synthesis of ZnO quantum dot/graphene nanocomposites by atomic layer deposition with high lithium storage capacity†

Xiang Sun,[a] Changgong Zhou,[b] Ming Xie,*[c] Hongtao Sun,[a] Tao Hu,[a] Fengyuan Lu,[a] Spencer M. Scott,[a] Steven M. George[c] and Jie Lian*[a]

Received 3rd February 2014
Accepted 24th February 2014

DOI: 10.1039/c4ta00589a

www.rsc.org/MaterialsA

Zinc oxide, as an inexpensive anode material, has attracted less attention than other metal oxides due to its poor cycling stability. A rational design of ZnO nanostructures with well-controlled particle sizes and microstructures is essential in order to improve their stability and performance as electrodes for lithium ion batteries (LIBs). Here, we demonstrate a simple approach *via* atomic layer deposition (ALD) to synthesize ZnO quantum dots (QDs) on graphene layers, in which the size of the ZnO QDs can be controlled from 2 to 7 nm by ALD cycles. A strong relationship between size and electrochemical performance is observed, in which smaller sized QDs on graphene display enhanced electrochemical performance. A high reversible specific capacity of 960 mA h g^{-1} is achieved at a current density of 100 mA g^{-1} for 2 nm ZnO QDs, approaching to the theoretical value of ZnO as the LIB anode. The greatly enhanced cycling stability and rate performance of the ALD ZnO QD/graphene composite electrode can be attributed to the well-maintained structural integrity without pulverization upon electrochemical charge/discharge for ZnO QDs with the grain size below a critical value.

Introduction

The development of portable electronic devices and hybrid electric cars requires advanced LIBs with large energy densities, fast rate capabilities, prolonged lifetimes, and low cost. However, the current commercial graphite anode has a low gravimetric capacity of 372 mA h g^{-1}, which leads to a limited output energy density of LIBs.[1] Transition metal oxides with higher theoretical capacities (>600 mA h g^{-1}), have been explored as alternative anode materials for high-performance LIBs, such as Fe_3O_4/Fe_2O_3,[2–4] Co_3O_4/CoO,[5–8] Mn_3O_4,[9] NiO,[10] MoO_3/MoO_2,[11,12] CuO,[13] and SnO_2.[14–16] However, the cost and abundance of those transition metal oxides have not been carefully examined for future practical large-scale production. The high cost of Co and Ni limits their potential application, and thus more attention should be focused on metal oxides, such as Fe, Mn, and Zn (see Table S1 in the ESI†).

Unlike Fe_2O_3/Fe_3O_4 and MnO_2, ZnO suffers from poor cyclability though its theoretical capacity (978 mA h g^{-1}) is nearly three times higher than that of graphite.[17,18] ZnO will transform to Zn upon the conversion reaction with Li^+, followed by the alloying reaction forming LiZn.[17,19] Similar to all of the other transition metal oxides, ZnO experiences a large volume expansion/contraction (~228%)[19] during discharge/charge processes. A recent *in situ* TEM study of ZnO nanowires has revealed that the lithium embrittlement of ZnO is much more severe as a result of nano-cracking rather than dislocation plasticity as observed in SnO_2.[20] As a result, the long-term stability of ZnO is much worse than that of SnO_2. A well-accepted routine to minimize such mechanical strain-induced cracking is to employ small particles at the nanoscale.[21,22] Different nanostructures have been explored to alleviate this detrimental volume change of ZnO, such as the hierarchical flower-like ZnO,[23] porous ZnO nanosheets,[20] ZnO nanorods,[24] and ZnO nanoparticles.[25] However, the particle sizes of these nanostructures are still too large, generally above 10 nm, leading to inferior capacity and cyclic performance. Therefore, synthesis of ZnO quantum dots (QDs) at a finer scale is crucial for the improvement of ZnO cycling performance, in which a critical size may exist to minimize the cracking issue. ZnO QDs have been widely studied for optoelectronics and solar cells,[26] however, they have not yet been reported as battery anodes.

Most common synthesis techniques for ZnO include cathodic deposition,[24] hydrothermal synthesis,[23,27] and magnetron sputtering.[28,29] It is difficult to control particle size down to

[a]Department of Mechanical, Aerospace & Nuclear Engineering, Rensselaer Polytechnic Institute, 110 8th Street Troy, NY 12180, USA. E-mail: lianj@rpi.edu

[b]Natural Science Department, Lawrence Technological University, Southfield, MI 48075, USA

[c]Department of Chemistry and Biochemistry and Department of Mechanical Engineering, University of Colorado at Boulder, Boulder, Colorado 80309, USA. E-mail: ming.xie@colorado.edu

† Electronic supplementary information (ESI) available: Table of $ per A h of metal oxides, schematic of ALD reactions, cycling performance of Al_2O_3–G, and detailed specific capacitance calculation of ZnO. See DOI: 10.1039/c4ta00589a

the nanometer region with a uniform particle distribution.[30–32] ALD, utilizing self-limited reactions occurring on the surface of a substrate, makes it possible to deposit nanoparticles on high-aspect-ratio substrates[33,34] or nanoparticles,[35,36] while controlling the particle size at the Angstrom scale.[37,38] Recently, ALD has been applied in depositing metal oxides on carbon substrates, showing great promise in lithium ion cathodes,[39] anodes,[40] and supercapacitors.[41,42]

Another issue with ZnO as the battery electrode is its relatively low electrical conductivity despite being more conductive than many metal oxides (~1 S cm^{-1} for ZnO[43] *vs.* 10^{-6} S cm^{-1} for other metal oxides). ZnO has been coupled with a variety of carbon substrates.[44,45] Graphene[46,47] is an excellent electronic conductor[48,49] with a high theoretical specific surface area of 2630 m^2 g^{-1},[50] high chemical stability,[46] and excellent mechanical properties.[51] The two-dimensional sheet structure of graphene also provides an excellent building block and an ideal conductive platform for accommodating nano-sized electrochemically active materials. However, due to its complex surface chemistry, graphene will interact with electrolytes at a high current density (such as 500 mA g^{-1}).[52,53] For example, graphene's oxygen-containing surface functional groups are very reactive and can oxidize the electrolyte and consequently induce electrochemical instability in the electrode. Additionally, graphene has a relatively low volumetric density (density of graphene powder <0.05 g cm^{-3}). Therefore, the synergy of combining metal oxides possessing much higher volumetric energy density and gravimetric capacity with graphene nanosheets is particularly attractive for developing advanced electrodes for LIBs. However, very limited results are reported for graphene–ZnO nanocomposites as anodes for lithium ion batteries. A previous study reported a specific capacity as low as 300 mA h g^{-1},[27] mainly due to mechanical degradation as a result of large particle sizes (30–40 nm).

In this work, we report the synthesis of uniform ZnO QDs with controllable sizes from 2 to 7 nm on graphene by ALD. The ZnO QDs are homogeneously anchored along the curvature of graphene sheets. The structural and electrochemical properties of the ZnO QD/graphene nanocomposites with different particle sizes were investigated. ZnO QDs with a particle size below 7 nm can be stably cycled; while smaller particles exhibit better rate performance. A near theoretical capacity can be achieved for ZnO with excellent cycling stability. The capacity fading of ZnO, resulting from the volume expansion-induced cracking, can be greatly mitigated by small size QDs with well-maintained structural integrity.

Experimental

Graphene sheets were produced by thermal exfoliation of the as-synthesized GO powders.[54] Details of the graphene synthesis and property characterization can be found in our previous publications.[42,55] ZnO ALD was grown directly on graphene powders using a rotary ALD reactor.[56,57] An ALD schematic can be found in the ESI.† Specifically, diethyl zinc ($Zn(CH_2CH_3)_2$) and high performance liquid chromatography (HPLC) grade H_2O were obtained from Sigma-Aldrich. ZnO ALD was performed at 120 °C using alternating $Zn(CH_2CH_3)_2$ and H_2O exposures in an ABAB… sequence:

$$ZnOH^* + Zn(CH_2CH_3)_2 \rightarrow ZnOZn(CH_2CH_3)^* + CH_3CH_3Zn(CH_2CH_3)^* + H_2O \rightarrow ZnOH^* + CH_3CH_3$$

where the asterisks represent the surface species. The typical growth rate for the ZnO ALD chemistry is ~2 Å per cycle,[58,59] and thus the particle of ZnO can be well controlled at the nanometer scale by ALD cycles. The ZnO ALD reaction sequence was: (i) $Zn(CH_3CH_2)_2$ dose to 1.0 Torr; (ii) evacuation of reaction products and excess $Zn(CH_3CH_2)_2$; (iii) H_2O dose to 1.0 Torr; and (iv) evacuation of reaction products and excess H_2O. Similar to carbon nanotubes, graphene has a low surface reactivity for ALD deposition, as the graphene basal plane is very unreactive, and thus it is difficult to nucleate ZnO on graphene. It is expected that ZnO will nucleate and grow at defects and edge planes of the graphene surface, resulting in a distribution of ZnO nanoparticles.

The phase, crystallinity, and microstructure of the ALD ZnO were characterized by a combination of material characterization approaches including XRD using a PANanalytical X-ray diffraction system, scanning electron microscopy by a Carl Zeiss Ultra 1540 Dual Beam FIB/SEM system, and transmission electron microscopy (TEM) using a JEOL JEM-2010 instrument operated at 200 kV. The surface area and pore size distribution were measured using a Quantachrome AUTOSORB-1 instrument, with the samples heated at 150 °C under vacuum for 12 hours before testing. Thermogravimetric analysis (TGA) was performed in air from 30 °C to 700 °C at a heating rate of 10 °C min^{-1} in a TGA Instrument (TGA-Q50).

The electrodes were prepared by mixing ZnO–G nanocomposites with polyvinylidene fluoride and carbon black at a weight ratio of 75 : 15 : 10 in 1-methyl-2-pyrrolidinone solvent. The slurry was coated on copper foil by using a blade and dried under vacuum at 80 °C overnight. All of the cells were assembled in an argon-filled dry box with Li metal as the negative electrode. A Celgard separator 2340 and 1 M $LiPF_6$ electrolyte solution in 1 : 1 w/w ethylene carbonate and diethyl carbonate (Novolyte) were used to fabricate the coin cells. Cyclic voltammetry (CV) measurement was carried out using a potentiostat VersaSTAT 4 (Princeton Applied Research) at a scan rate of 0.5 mV s^{-1}. Galvanostatic charge/discharge cycles were performed at a voltage range of 2.5–0.05 V using an Arbin BT 2000 testing station.

Results and discussion

Graphene nanosheets were prepared by thermal exfoliation of graphite oxide (GO), and therefore, defects and residual oxygen functional groups inevitably exist in the structure of graphene. These defective sites serve as the initial nucleation sites for the controllable growth of ZnO QDs by ALD. The mesoporous structure developed upon thermal exfoliation[42] allows the gas phase ALD precursors to diffuse into the internal structures of graphene, resulting in well-distributed ZnO QDs.

As observed from SEM analysis (Fig. 1), the ZnO QDs are uniformly anchored along the porous network of wrinkled graphene. No uncoated graphene surface can be seen after deposition at longer cycles. The high coverage of surface defects (carboxyl or hydroxyl groups) on graphene allows uniform surface interaction with ALD precursors. The typical sizes of ZnO QDs after 15, 30, and 50 ALD cycles are ~2 nm, ~4 nm, and ~7 nm in diameter, respectively. The average diameter of ZnO increases nearly proportionally to the number of repeated ALD cycles. This result suggests that the time for diffusion of the ALD precursors into the porous structure of graphene is sufficient and therefore the growth rate is nearly linear, one of the distinctive advantages for ALD. After 50 ALD cycles, ZnO QDs begin to converge into dense films, as evidenced by the significant increase in the thickness of the graphene sheet. A high resolution TEM image shows a basal plane of 0.28 nm, matching well with the (100) inter-planar spacing of ZnO, confirming the crystalline nature of ZnO by ALD. From the structural analysis, crystallized ZnO nanoparticles are uniformly deposited by ALD throughout the three dimensional network of graphene.

The degree of crystallinity of ZnO on graphene was further examined by XRD. Fig. 2(a) shows the XRD patterns of the ZnO–G composites synthesized at different ALD cycles. The sharp peaks can be assigned to the hexagonal structure of ZnO (JCPDS01-076-0704) and a weak broadened peak at 23–27° can be ascribed to the (002) plane of the disordered graphene sheets.[42,55] This is consistent with other ZnO ALD literature studies that ZnO ALD intends to form a crystalline structure even at room temperature.[60] In addition, it is well-studied that the ZnO ALD process easily produces stoichiometric binary films without measurable amounts of impurities such as carbon or oxygen.[61] As the number of the ALD cycles increased, the ZnO diffraction peaks become more obvious and sharper, indicating the crystal growth by repeated ALD cycles.

TGA measurements as shown in Fig. 2(b) indicate that the mass percentages of ZnO in the composites are 42.7%, 68.2%, and 87% for 15, 30, and 50 ALD cycles, respectively. The high mass loading of the active material is critical to realize the feasibility of using ALD for large-scale nanocomposite powder production. Here we adapted static dosing ALD precursors instead of flow-type ALD,[37,38] since static dosing can reach a much higher reactant utilization efficiency and allow to coat high surface area substrates, such as graphene and CNT powders.[56] Our results indicate that more than 80 wt% of active materials can be achieved with less than 50 ALD cycles. The greatly reduced ALD deposition time and cost, along with maximized precursor utilization efficiency make ALD suitable for large-scale production. At this time, we have the capability of synthesizing nanocomposites in a batch quantity of 10 g powder per ALD run at a lab scale.

The nitrogen adsorption/desorption isotherms of ZnO–G composites together with the pore size distribution, derived

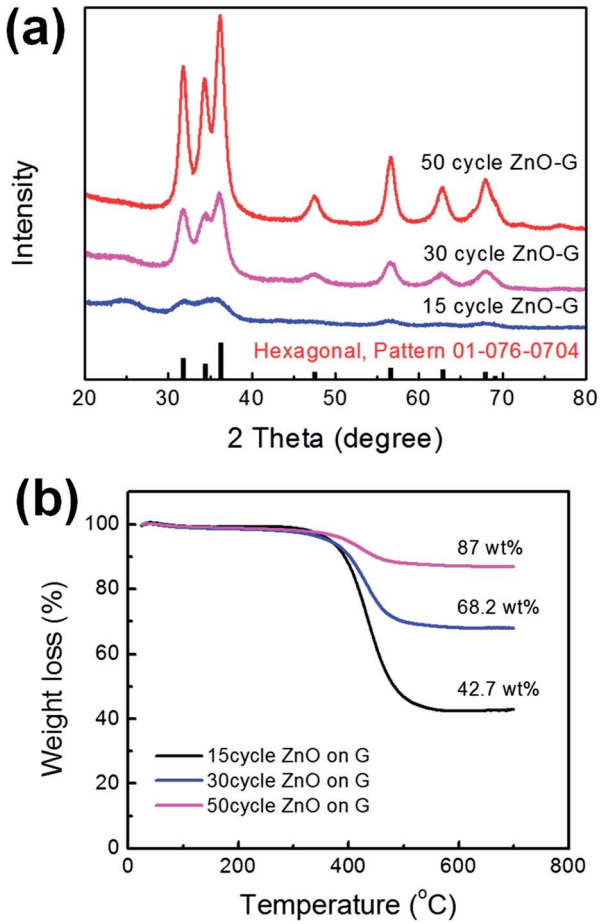

Fig. 2 (a) XRD patterns and (b) TGA of the ALD ZnO–G composites.

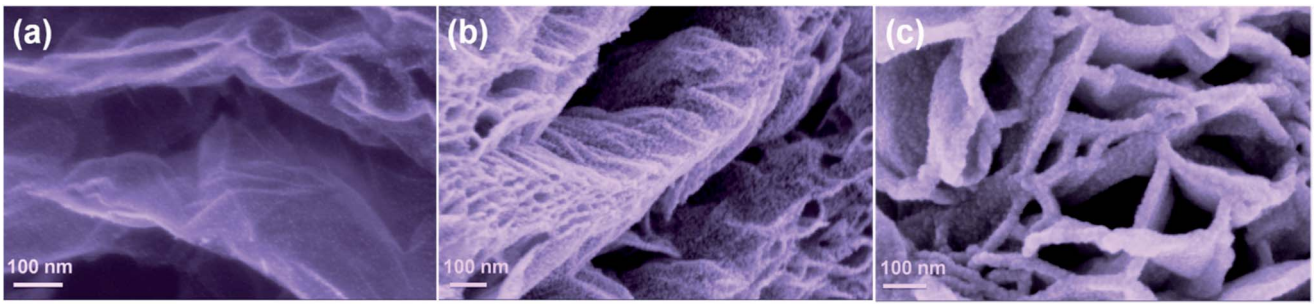

Fig. 1 SEM images showing the morphology of graphene nanosheets coated by ZnO QDs at different ALD cycles: (a) 15 ALD cycles, (b) 30 ALD cycles, and (c) 50 ALD cycles.

based on the Density Functional Theory (DFT) model, are shown in Fig. 3. All three samples display the typical type IV isotherm with a large hysteresis loop, demonstrating that a significant amount of meso-pores initially existing in the graphene[42] were preserved after ALD depositions. The broad pore distribution from 3–35 nm almost remains intact after deposition, resulting from the unique self-limiting reaction of ALD. Such an open structure is expected to provide easy access of electrolytes and facilitate fast Li-ion diffusion when used as a potential lithium-ion battery electrode. The specific surface areas are 314.5, 138.8, and 27.2 $m^2\ g^{-1}$ for 15, 30, and 50 ALD cycles ZnO–G composites, respectively, as a result of the overall reduction in the specific area with increased mass loadings of ZnO.

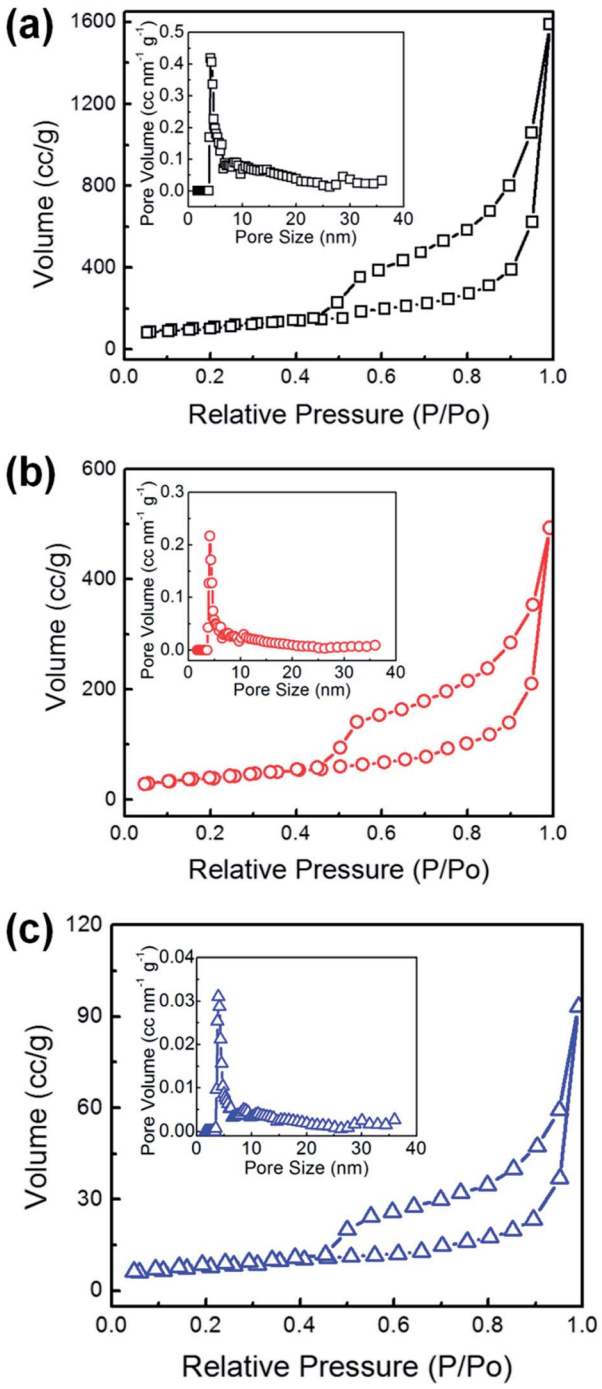

Fig. 3 Nitrogen adsorption/desorption isotherms of the ALD ZnO–G composites grown using (a) 15, (b) 30, and (c) 50 cycles, and the insets are the corresponding DFT pore size distributions.

Electrodes made with the ZnO–G nanocomposites were tested in coin cells with lithium metal as a counter electrode. Cyclic voltammograms (CVs) of the ZnO–G nanocomposites were measured between 0.01 and 3 V at a scan rate of 0.5 mV s^{-1}. As shown in Fig. 4(a), in the first cathodic scan, a strong peak at ~0.11 V was observed and can be ascribed to the reduction of ZnO to Zn and the formation of LiZn alloy, as well as the formation and growth of solid electrolyte interphase (SEI).[20] These peaks overlap each other, and therefore only one strong peak can be seen. The high current response near 0 V indicates lithium intercalation into the graphene backbone.[5,8] In the subsequent cathodic scans, the major peak splits into two peaks concentrated at 0.7 and 0.1 V, corresponding to the reduction of ZnO to Zn and alloy formation of lithium and zinc,[24] respectively. These peaks tend to be stabilized in the subsequent cycles. On the anodic side, a broad shoulder exists between 0.2 and 0.4 V, and two small peaks located at 0.52 and 0.66 V, can be attributed to the multi-step delithiation of LiZn through LiZn → Li_2Zn_3 → $LiZn_2$ → Li_2Zn_5 → Zn.[18,62] In addition, a broad peak is found at ~1.38 V and can be related to the formation of ZnO by the redox reaction between Zn and Li_2O.[63,64] The anodic curves also show good reproducibility in the subsequent cycles, suggesting a high reversibility of the lithium and ZnO reactions. From the CV analysis, the overall lithium storage reaction of ZnO can be described as ZnO + 2Li + $2e^-$ ↔ Zn + Li_2O and Zn + Li^+ + e^- ↔ ZnLi.

Fig. 4(b) and (c) present the voltage profiles of 15 and 30 ALD cycle ZnO–G composites in the 1st, 5th, 10th, 30th, and 50th cycles at a current density of 100 mA g^{-1}. The initial discharge capacity is 2000 mA h g^{-1} for 15 ALD cycle ZnO–G which decreased to 728 mA h g^{-1} at the 5th cycle. In comparison, the 30 ALD cycle ZnO–G delivered a discharge capacity of 1400 and 615 mA h g^{-1} at the first and the fifth cycles, respectively. The capacity degradation is reduced in subsequent cycles and a stable capacity is nearly preserved after 5 cycles. The large irreversible initial capacity loss can be attributed to the electrolyte decomposition and SEI formation. As revealed in a previous study, SEI formation is linearly proportional to the BET specific surface area of carbon-based materials.[65] Increasing the ZnO particle size by exposing graphene to a larger number of ALD cycles decreases the specific surface area which in turn decreases the initial irreversible capacity loss. Similar lithium storage behaviors were observed for two composites with different ALD cycles. A large plateau was observed at 0.8 V in the first discharge, which corresponds to the SEI formation and reduction of ZnO into Zn, followed by a sloping down to 0.05 V corresponding to the subsequent alloy formation[23,27,44] and lithium intercalation into graphene.[66] A voltage plateau at ~1.2 V was observed from the charging curves, indicating that the oxidation reaction of Zn with Li_2O,[67] is consistent with the CV analysis.

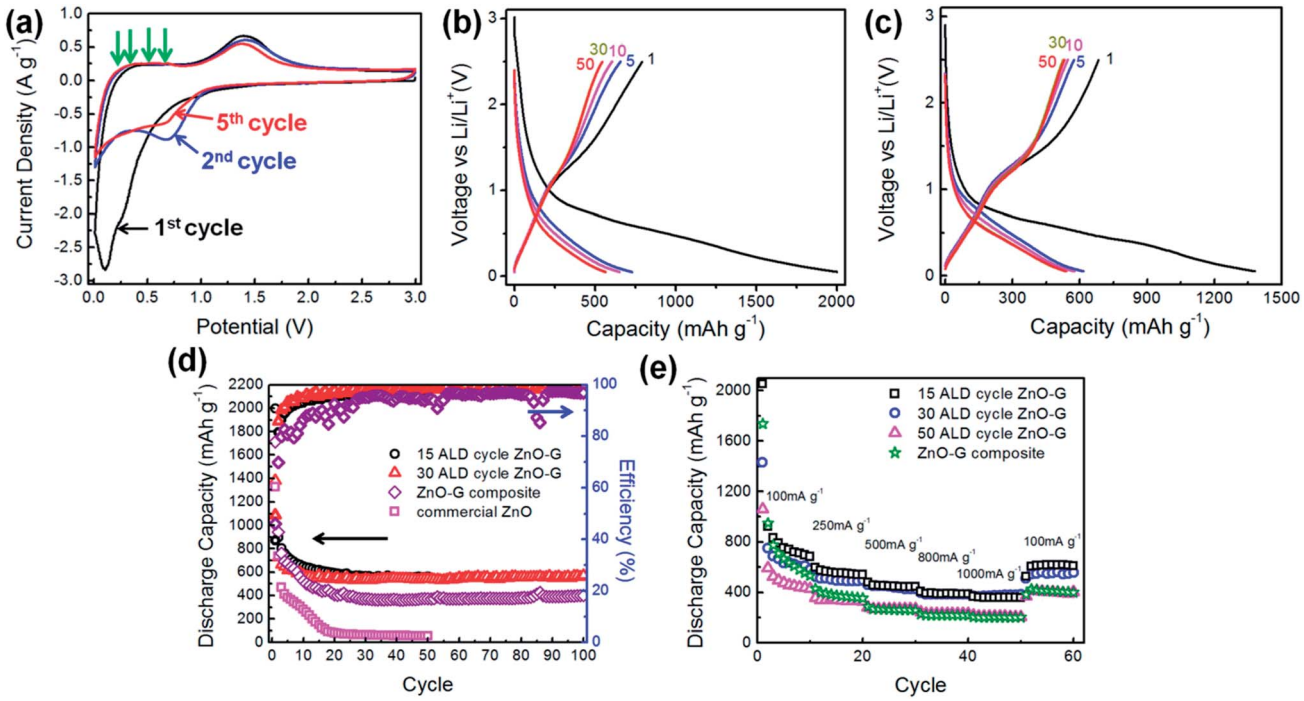

Fig. 4 Electrochemical performance of the ALD ZnO/G composites: (a) CV curves of 15 ALD cycle ZnO–G composite; galvanostatic charge/discharge curves at a current density of 100 mA g^{-1} for (b) 15 ALD cycle ZnO–G and (c) 30 ALD cycle ZnO–G; (d) cycling performance at 100 mA g^{-1} of the ALD ZnO–G composites and comparison with commercial ZnO nanoparticles and a controlled electrode by mechanically-mixing graphene and ZnO nanoparticles; and (e) rate performance of ZnO–G composites at various current densities.

The long term cyclic stability of the ALD ZnO/G composite electrodes was evaluated at a current density of 100 mA g^{-1} for 100 cycles. For comparison, an electrode prepared from commercial ZnO nanoparticles with a size of 20 nm and a surface area of 50 m^2 g^{-1} acquired from Nanostructured & Amorphous Materials, Inc. was also cycled at the same current density. In addition, a control experiment was designed with a reference electrode (denoted as ZnO–G composite) prepared by mechanically mixing commercial ZnO nanoparticles with graphene, and the weight percentage of the controlled electrode resembles that of the 30 ALD cycle ZnO–G composite electrode with 68% ZnO and 32% graphene. As shown in Fig. 4(d), the reversible capacity of commercial ZnO nanoparticles continuously decayed from the 1st to the 50th cycle, and exhibited a capacitance less than 20 mA h g^{-1} after 20 cycles. The control sample has much higher capacity ~400 mA h g^{-1} due to the contribution from extra graphene. In comparison, the 15 and 30 ALD cycle ZnO–G nanocomposites exhibit stable discharge capacities of 560 mA h g^{-1} and 540 mA h g^{-1} even after 50 and 100 deep cycles, respectively. The Coulombic efficiency reaches 97.6% and 98.1% for 15 ALD cycle ZnO–G in the 50th cycle and the 30th ALD cycle ZnO–G in the 100th cycle, respectively.

It was reported that the defects and edge plane in the graphene structure significantly contributed to the lithium storage capacity.[68] However, those sites preferably attracted ALD precursors as compared to the graphene basal planes which are very inert to ALD precursors. Therefore, the capacity contribution from those defects and edge planes of graphene was restricted since they were covered with ZnO QDs. To obtain the real capacitance contribution of graphene, 5 ALD cycles of Al_2O_3 were deposited on graphene powders and the charge/discharge cycles were carried out under the same condition. The typical growth rate of ALD Al_2O_3 is 0.1 nm per cycle[69] and therefore ~0.5 nm Al_2O_3 particles formed on graphene. The Al_2O_3 mimicked the ZnO deposited at the defects and edge planes of graphene, in that only intercalation between graphene layers can contribute to the capacitance of this composite. As shown in Fig. S1,† the stable capacity of Al_2O_3–G after 50 deep cycles is only 258 mA h g^{-1}. Therefore, the ZnO contribution in the composite can be extracted after considering the real

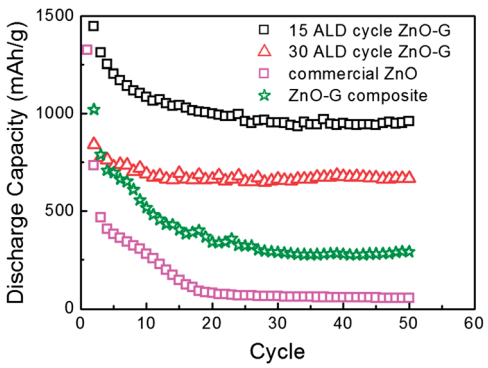

Fig. 5 Specific capacity of ZnO only in ALD ZnO–G composites at 100 mA g^{-1} as compared with ZnO–G composites and commercial ZnO nanoparticles. A nearly theoretical capacity (960 mA h g^{-1}) of ZnO can be achieved for 15 ALD cycle ZnO/graphene with the QD size of 2 nm.

Table 1 Comparison of ZnO battery performance with this work (1 C = 978 mA g^{-1})

ZnO nanostructures	Stable capacity	Capacity at high rate
ZnO nanocrystals on graphene[27]	~300 mA h g^{-1} at 50 mA g^{-1} after 25 cycles	N.A.
Au/ZnO nanoflowers[23]	~392 mA h g^{-1} at 120 mA g^{-1} after 50 cycles	N.A.
Porous ZnO nanosheets on copper[20]	~400 mA h g^{-1} at 500 mA g^{-1} after 100 cycles	~300 mA h g^{-1} at 1A g^{-1}
Nanosized ZnO in carbon[45]	~700 mA h g^{-1} at 100 mA g^{-1} after 100 cycles (based on the weight of ZnO)	N.A.
Zn–Al_2O_3–C nanocomposites[70]	~380 mA h g^{-1} at 100 mA g^{-1} after 50 cycles	N.A.
ZnO thin films[17]	~220 mA h g^{-1} at 20 μA cm^{-2} after 40 cycles	N.A.
Flower-like ZnO–NiO–C films[71]	~488 mA h g^{-1} at 0.5 C after 50 cycles	~380 mA h g^{-1} at 1 C
Carbon/ZnO nanorod arrays[44]	~330 mA h g^{-1} at 0.25 C after 50 cycles	N.A.
Ni-coated ZnO[67]	~490 mA h g^{-1} at 80 mA g^{-1} after 30 cycles	N.A.
ZnO nanorod arrays[24]	~310 mA h g^{-1} at 0.1 mA cm^{-2} after 40 cycles	N.A.
This work	~540 mA h g^{-1} at 100 mA g^{-1} after 100 cycles ~960 mA h g^{-1} (based on the weight of ZnO)	~400 mA h g^{-1} at 1A g^{-1}

contribution from graphene (see detailed calculations in the ESI†). As shown in Fig. 5, the specific capacitances of ZnO in 15 and 30 ALD cycle ZnO–G nanocomposites after 50 cycles are 960 and 660 mA h g^{-1}, respectively. The stable capacity of 960 mA h g^{-1} nearly approaches the theoretical value of ZnO (978 mA h g^{-1}) and to the best of our knowledge, is the highest-reported value in the literature for ZnO-based anodes (Table 1).

Excellent rate performance has also been achieved using 15, 30, and 50 ALD cycle ZnO–G nanocomposites, as shown in Fig. 4(e) at various current densities. The cell has been continuously cycled without any pause between different rates. Impressively, 15 and 30 ALD cycle ZnO–G nanocomposites both maintain ~400 mA h g^{-1} capacity even when the current density is increased to 1000 mA g^{-1}, retaining ~66% and ~74% of their discharge capacity at 100 mA g^{-1}, respectively. The reference electrode only reaches ~200 mA h g^{-1} capacity cycled at the same current density 1000 mA g^{-1}. In addition, the initial decay for the reference electrode is more severe than any of the ALD ZnO–G nanocomposites. These results indicate that chemically-bonded nanocomposites by ALD have much better rate performance than the mechanically-mixed control sample. Although the control electrode has more capacity contributed from higher graphene loading, than the 50 ALD cycle ZnO–G nanocomposites, their rate performances are almost identical.

The excellent electrochemical performance of the ZnO–G nanocomposites can be attributed to several potential factors: (1) ALD allows for the deposition of ZnO QDs under the critical size below which the pulverization of large ZnO QDs (228% volume expansion/contraction during discharge/charge processes) can be greatly mitigated; (2) ultra-small ZnO QDs shorten the Li^+ diffusion path, resulting in a very impressive rate performance; (3) the 3-D structure of ZnO–G nanocomposites will greatly enhance lithium diffusion and electron conduction; (4) excellent mechanical properties of graphene[51] can accommodate the large volume change of ZnO; and (5) the chemical bonding between ZnO and graphene prevents the aggregation of nanoparticles during cycling.

To illustrate the advantages of controlling smaller-sized QDs to mitigate the mechanical degradation, and thus capacity fading, the microstructure of the ZnO QDs upon cycling was characterized in detail by TEM. Fig. 6 shows the TEM image of 50 ALD cycle ZnO–G before and after 50 cycles at 100 mA g^{-1}. No obvious fracture or agglomeration of the nanoparticles were observed, suggesting that 7 nm ZnO on a graphene substrate is below the critical size for pulverization. The failure of the electrode made from commercial ZnO nanoparticles is most likely due to relatively large particle sizes. This phenomenon has been observed in SnO_2 and Si by *in situ* TEM with ionic liquids.[72] This is the first time that a similar size effect has been observed for ZnO in a coin cell configuration with an organic electrolyte. It should be noted that the integration of the graphene and metal oxides by ALD may further enhance the stability of metal oxide QDs, greatly improving the rate performance of the composite electrodes. Our study also suggests that precise thickness control of ALD allows us to explore critical sizes for other potential electrode materials, which suffer pulverization during cycling within a real battery device.

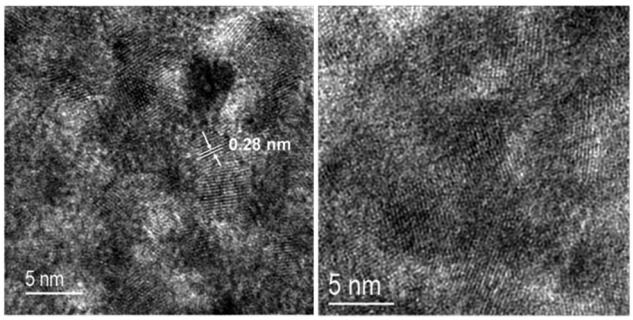

Fig. 6 TEM images of 50 ALD cycle ZnO–G composites before (left) and after (right) cycling. No fracture or grain coarsening was observed upon cycling, suggesting well maintained structural integrity of QDs with the size of ~7 nm.

Conclusions

In this study, we have successfully synthesized ZnO quantum dots on graphene with well controlled particle sizes by controlling ALD cycles, and demonstrated that the smaller sized

particles of the ZnO–G composite electrodes contribute towards better electrochemical performance. Electrochemical measurements indicated that the 15 ALD cycle of ZnO–G with a particle size of 2 nm exhibits a stable capacity of 560 mA h g^{-1} at 100 mA g^{-1} and 400 mA h g^{-1} at 1000 mA g^{-1}. By subtracting the graphene contribution from the composites, ZnO QDs display an unprecedented specific capacity of 960 mA h g^{-1}, approaching the theoretical capacity of 978 mA h g^{-1}. The excellent capacity and rate performance of the ZnO–G composite can be attributed to the small-sized QDs. In comparison, the pulverization of large particles typically occurs as a result of minimization of significant volume expansion. These results highlight the importance of fine control and manipulation of the microstructure and particle size to improve electrode electrochemical performance.

Acknowledgements

This work is supported by the National Science Foundation under an award of DMR 1151028. The work done at the University of Colorado was supported by the Defense Advanced Research Project Agency (DARPA).

Notes and references

1 J. M. Tarascon and M. Armand, *Nature*, 2001, **414**, 359–367.
2 G. M. Zhou, D. W. Wang, F. Li, L. L. Zhang, N. Li, Z. S. Wu, L. Wen, G. Q. Lu and H. M. Cheng, *Chem. Mater.*, 2010, **22**, 5306–5313.
3 L. W. Ji, Z. K. Tan, T. R. Kuykendall, S. Aloni, S. D. Xun, E. Lin, V. Battaglia and Y. G. Zhang, *Phys. Chem. Chem. Phys.*, 2011, **13**, 7139–7146.
4 X. J. Zhu, Y. W. Zhu, S. Murali, M. D. Stollers and R. S. Ruoff, *ACS Nano*, 2011, **5**, 3333–3338.
5 Z. S. Wu, W. C. Ren, L. Wen, L. B. Gao, J. P. Zhao, Z. P. Chen, G. M. Zhou, F. Li and H. M. Cheng, *ACS Nano*, 2010, **4**, 3187–3194.
6 B. J. Li, H. Q. Cao, J. Shao, G. Q. Li, M. Z. Qu and G. Yin, *Inorg. Chem.*, 2011, **50**, 1628–1632.
7 H. Kim, D. H. Seo, S. W. Kim, J. Kim and K. Kang, *Carbon*, 2011, **49**, 326–332.
8 C. X. Peng, B. D. Chen, Y. Qin, S. H. Yang, C. Z. Li, Y. H. Zuo, S. Y. Liu and J. H. Yang, *ACS Nano*, 2012, **6**, 1074–1081.
9 H. L. Wang, L. F. Cui, Y. A. Yang, H. S. Casalongue, J. T. Robinson, Y. Y. Liang, Y. Cui and H. J. Dai, *J. Am. Chem. Soc.*, 2010, **132**, 13978–13980.
10 Y. Q. Zou and Y. Wang, *Nanoscale*, 2011, **3**, 2615–2620.
11 Y. Xu, R. Yi, B. Yuan, X. F. Wu, M. Dunwell, Q. L. Lin, L. Fei, S. G. Deng, P. Andersen, D. H. Wang and H. M. Luo, *J. Phys. Chem. Lett.*, 2012, **3**, 309–314.
12 T. Tao, A. M. Glushenkov, C. F. Zhang, H. Z. Zhang, D. Zhou, Z. P. Guo, H. K. Liu, Q. Y. Chen, H. P. Hu and Y. Chen, *J. Mater. Chem.*, 2011, **21**, 9350–9355.
13 B. Wang, X. L. Wu, C. Y. Shu, Y. G. Guo and C. R. Wang, *J. Mater. Chem.*, 2010, **20**, 10661–10664.
14 D. H. Wang, R. Kou, D. Choi, Z. G. Yang, Z. M. Nie, J. Li, L. V. Saraf, D. H. Hu, J. G. Zhang, G. L. Graff, J. Liu, M. A. Pope and I. A. Aksay, *ACS Nano*, 2010, **4**, 1587–1595.
15 S. M. Paek, E. Yoo and I. Honma, *Nano Lett.*, 2009, **9**, 72–75.
16 L. S. Zhang, L. Y. Jiang, H. J. Yan, W. D. Wang, W. Wang, W. G. Song, Y. G. Guo and L. J. Wan, *J. Mater. Chem.*, 2010, **20**, 5462–5467.
17 Z. W. Fu, F. Huang, Y. Zhang, Y. Chu and Q. Z. Qin, *J. Electrochem. Soc.*, 2003, **150**, A714–A720.
18 J. P. Liu, Y. Y. Li, X. T. Huang, G. Y. Li and Z. K. Li, *Adv. Funct. Mater.*, 2008, **18**, 1448–1458.
19 H. Usui, T. Kono and H. Sakaguchi, *Int. J. Electrochem. Sci.*, 2012, **7**, 4322–4334.
20 A. Kushima, X. H. Liu, G. Zhu, Z. L. Wang, J. Y. Huang and J. Li, *Nano Lett.*, 2011, **11**, 4535–4541.
21 Z. Y. Zhou, N. Tian, J. T. Li, I. Broadwell and S. G. Sun, *Chem. Soc. Rev.*, 2011, **40**, 4167–4185.
22 P. G. Bruce, B. Scrosati and J. M. Tarascon, *Angew. Chem., Int. Ed.*, 2008, **47**, 2930–2946.
23 M. Ahmad, Y. Y. Shi, A. Nisar, H. Y. Sun, W. C. Shen, M. Wei and J. Zhu, *J. Mater. Chem.*, 2011, **21**, 7723–7729.
24 H. B. Wang, Q. M. Pan, Y. X. Cheng, J. W. Zhao and G. P. Yin, *Electrochim. Acta*, 2009, **54**, 2851–2855.
25 C. Li, Z. S. Yu, S. M. Fang, H. X. Wang, Y. H. Gui, J. Q. Xu and R. F. Chen, *J. Alloys Compd.*, 2009, **475**, 718–722.
26 V. A. Fonoberov, K. A. Alim, A. A. Balandin, F. Xiu and J. Liu, *Phys. Rev. B: Condens. Matter Mater. Phys.*, 2006, **73**, 165317.
27 W. T. Song, J. Xie, S. Y. Liu, Y. X. Zheng, G. S. Cao, T. J. Zhu and X. B. Zhao, *Int. J. Electrochem. Sci.*, 2012, **7**, 2164–2174.
28 H. Q. Dai, H. Xu, Y. N. Zhou, F. Lu and Z. W. Fu, *J. Phys. Chem. C*, 2012, **116**, 1519–1525.
29 J. Xie, N. Imanishi, A. Hirano, Y. Takeda, O. Yamamoto, X. B. Zhao and G. S. Cao, *Thin Solid Films*, 2011, **519**, 3373–3377.
30 J. H. Liu, J. S. Chen, X. F. Wei, X. W. Lou and X. W. Liu, *Adv. Mater.*, 2011, **23**, 998–1002.
31 D. H. Wang, D. W. Choi, J. Li, Z. G. Yang, Z. M. Nie, R. Kou, D. H. Hu, C. M. Wang, L. V. Saraf, J. G. Zhang, I. A. Aksay and J. Liu, *ACS Nano*, 2009, **3**, 907–914.
32 G. F. Cao, Y. Liao, X. H. Zhang and J. H. Chen, *Acta Phys.–Chim. Sin.*, 2011, **27**, 1679–1684.
33 J. W. Elam, D. Routkevitch, P. P. Mardilovich and S. M. George, *Chem. Mater.*, 2003, **15**, 3507–3517.
34 R. G. Gordon, D. Hausmann, E. Kim and J. Shepard, *Chem. Vap. Deposition*, 2003, **9**, 73–78.
35 J. A. McCormick, K. P. Rice, D. F. Paul, A. W. Weimer and S. M. George, *Chem. Vap. Deposition*, 2007, **13**, 491–498.
36 J. D. Ferguson, A. W. Weimer and S. M. George, *Thin Solid Films*, 2000, **371**, 95–104.
37 C. Kim, M. Noh, M. Choi, J. Cho and B. Park, *Chem. Mater.*, 2005, **17**, 3297–3301.
38 H. Kim, M. Seo, M. H. Park and J. Cho, *Angew. Chem., Int. Ed.*, 2010, **49**, 2146–2149.
39 X. Y. Chen, H. L. Zhu, Y. C. Chen, Y. Y. Shang, A. Y. Cao, L. B. Hu and G. W. Rubloff, *ACS Nano*, 2012, **6**, 7948–7955.
40 X. F. Li, X. B. Meng, J. Liu, D. S. Geng, Y. Zhang, M. N. Banis, Y. L. Li, J. L. Yang, R. Y. Li, X. L. Sun, M. Cai and M. W. Verbrugge, *Adv. Funct. Mater.*, 2012, **22**, 1647–1654.

41 S. Boukhalfa, K. Evanoff and G. Yushin, *Energy Environ. Sci.*, 2012, **5**, 6872–6879.
42 X. Sun, M. Xie, G. K. Wang, H. T. Sun, A. S. Cavanagh, J. J. Travis, S. M. George and J. Lian, *J. Electrochem. Soc.*, 2012, **159**, A364–A369.
43 M. Schuisky, J. W. Elam and S. M. George, *Appl. Phys. Lett.*, 2002, **81**, 180–182.
44 J. P. Liu, Y. Y. Li, R. M. Ding, J. Jiang, Y. Y. Hu, X. X. Ji, Q. B. Chi, Z. H. Zhu and X. T. Huang, *J. Phys. Chem. C*, 2009, **113**, 9008.
45 O. B. Chae, S. Park, J. H. Ryu and S. M. Oh, *J. Electrochem. Soc.*, 2013, **160**, A11–A14.
46 A. K. Geim and K. S. Novoselov, *Nat. Mater.*, 2007, **6**, 183–191.
47 K. S. Novoselov, A. K. Geim, S. V. Morozov, D. Jiang, Y. Zhang, S. V. Dubonos, I. V. Grigorieva and A. A. Firsov, *Science*, 2004, **306**, 666–669.
48 S. Stankovich, D. A. Dikin, G. H. B. Dommett, K. M. Kohlhaas, E. J. Zimney, E. A. Stach, R. D. Piner, S. T. Nguyen and R. S. Ruoff, *Nature*, 2006, **442**, 282–286.
49 J. R. Miller, R. A. Outlaw and B. C. Holloway, *Science*, 2010, **329**, 1637–1639.
50 M. D. Stoller, S. J. Park, Y. W. Zhu, J. H. An and R. S. Ruoff, *Nano Lett.*, 2008, **8**, 3498–3502.
51 A. K. Geim, *Science*, 2009, **324**, 1530–1534.
52 M. Winter, *Z. Phys. Chem.*, 2009, **223**, 1395–1406.
53 W. A. V. Schalkwijk and B. Scrosati, *Advances in lithium-ion batteries*, Kluwer Academic/Plenum Publishers, New York, NY, 2002.
54 M. J. McAllister, J. L. Li, D. H. Adamson, H. C. Schniepp, A. A. Abdala, J. Liu, M. Herrera-Alonso, D. L. Milius, R. Car, R. K. Prud'homme and I. A. Aksay, *Chem. Mater.*, 2007, **19**, 4396–4404.
55 G. K. Wang, X. Sun, F. Y. Lu, Q. K. Yu, C. S. Liu and J. Lian, *J. Solid State Chem.*, 2012, **185**, 172–179.
56 J. A. McCormick, B. L. Cloutier, A. W. Weimer and S. M. George, *J. Vac. Sci. Technol., A*, 2007, **25**, 67–74.
57 A. S. Cavanagh, C. A. Wilson, A. W. Weimer and S. M. George, *Nanotechnology*, 2009, **20**, 255602.
58 V. Lujala, J. Skarp, M. Tammenmaa and T. Suntola, *Appl. Surf. Sci.*, 1994, **82–83**, 34–40.
59 A. Yamada, B. Sang and M. Konagai, *Appl. Surf. Sci.*, 1997, **112**, 216–222.
60 J. Malm, E. Sahramo, J. Perala, T. Sajavaara and M. Karppinen, *Thin Solid Films*, 2011, **519**, 5319–5322.
61 J. T. Tanskanen, J. R. Bakke, T. A. Pakkanen and S. F. Bent, *J. Vac. Sci. Technol., A*, 2011, **29**, 031507.
62 F. Belliard and J. T. S. Irvine, *J. Power Sources*, 2001, **97–98**, 219–222.
63 H. Li, X. J. Huang and L. Q. Chen, *Solid State Ionics*, 1999, **123**, 189–197.
64 Y. Sharma, N. Sharma, G. V. S. Rao and B. V. R. Chowdari, *Adv. Funct. Mater.*, 2007, **17**, 2855–2861.
65 M. Winter, P. Novak and A. Monnier, *J. Electrochem. Soc.*, 1998, **145**, 428–436.
66 E. Yoo, J. Kim, E. Hosono, H. Zhou, T. Kudo and I. Honma, *Nano Lett.*, 2008, **8**, 2277–2282.
67 C. Q. Zhang, J. P. Tu, Y. F. Yuan, X. H. Huang, X. T. Chen and F. Mao, *J. Electrochem. Soc.*, 2007, **154**, A65–A69.
68 M. Pumera, *Energy Environ. Sci.*, 2011, **4**, 668–674.
69 J. W. Elam, M. D. Groner and S. M. George, *Rev. Sci. Instrum.*, 2002, **73**, 2981–2987.
70 X. H. Liu, Y. Liu, A. Kushima, S. Zhang, T. Zhu, J. Li and J. Y. Huang, *Adv. Energy Mater.*, 2012, **2**, 722–741.
71 Y. Hwa, J. H. Sung, B. Wang, C. M. Park and H. J. Sohn, *J. Mater. Chem.*, 2012, **22**, 12767–12773.
72 Q. M. Pan, L. M. Qin, J. Liu and H. B. Wang, *Electrochim. Acta*, 2010, **55**, 5780–5785.

